

PolyFly: Polytopic Optimal Planning for Collision-Free Cable-Suspended Aerial Payload Transportation

Mrunal Sarvaiya¹, Guanrui Li², and Giuseppe Loianno¹



Fig. 1: A quadrotor with a suspended payload navigating through cluttered environments. The left and middle images show different perspectives of Environment 3, where the system maneuvers around multiple obstacles. The right image depicts Environment 7, where the system successfully passes through a narrow gap—just wide enough for the cable—demonstrating the planner’s ability to exploit the geometry of individual components.

Abstract—Aerial transportation robots using suspended cables have emerged as versatile platforms for disaster response and rescue operations. To maximize the capabilities of these systems, robots need to aggressively fly through tightly constrained environments, such as dense forests and structurally unsafe buildings, while minimizing flight time and avoiding obstacles. Existing methods geometrically over-approximate the vehicle and obstacles, leading to conservative maneuvers and increased flight times. We eliminate these restrictions by proposing PolyFly, an optimal global planner which considers a non-conservative representation for aerial transportation by modeling each physical component of the environment, and the robot (quadrotor, cable and payload), as independent polytopes. We further increase the model accuracy by incorporating the attitude of the physical components by constructing orientation-aware polytopes. The resulting optimal control problem is efficiently solved by converting the polytope constraints into smooth differentiable constraints via duality theory. We compare our method against the existing state-of-the-art approach in eight maze-like environments and show that PolyFly produces faster trajectories in each scenario. We also experimentally validate our proposed approach on a real quadrotor with a suspended payload, demonstrating the practical reliability and accuracy of our method.

I. INTRODUCTION

Micro Aerial Vehicles (MAVs), particularly quadrotors equipped with cable-suspended payload systems, have gained significant attention due to their versatility and effectiveness in diverse applications such as inspection [1], search and rescue missions [2], and package transportation [3]. Their ability to deliver essential materials in regions inaccessible by ground robots makes them invaluable during disaster

relief operations [4]. Furthermore, aerial transportation systems offer considerable advantages in energy efficiency over ground vehicles for last-mile logistics, significantly reducing environmental footprints in urban delivery contexts [5].

In time critical scenarios, such as rescue missions, it is crucial for aerial vehicles to optimize their flight path to reduce the mission time, especially in challenging environments like dense forests or earthquake-damaged and structurally unsafe buildings. This requires the robot planners to avoid obstacles while maneuvering through narrow gaps and around tight corners, which need non-conservative physical approximations of the system components. Furthermore, unlike standalone quadrotor methods, aerial transportation planners must take into account the increased complexity of the configuration space introduced by the swinging payload.

Existing methods often simplify these systems into spheres [6] or large prisms [7], [8] to address computational demands, trading off solution quality for computational speed. In contrast, our approach directly addresses these limitations by representing each component - quadrotor, payload, and cable — as distinct polytopes. We further enhance our planner by incorporating the quadrotor’s orientation into the polytopic representation. This orientation-aware modeling enables more precise collision prediction during aggressive maneuvers in confined spaces such as the environment shown in Fig. 5. This representation provides planners with detailed geometric information, enhancing their capabilities to navigate maze-like and highly constrained environments.

Current aerial transportation planning methodologies can broadly be categorized into sampling-based and optimization-based approaches. Within optimization methods, trajectories are either parameterized through polynomial representations [6], [9] or discretized and solved via Model Predictive Control (MPC) frameworks [7], [10]–[12]. Our work builds upon MPC-based global planning techniques

¹The authors are with the University of California Berkeley, Department of Electrical Engineering and Computer Sciences, Berkeley, CA 94720, USA. email: {mrunaljsarvaiya, loiannog}@eecs.berkeley.edu.

²The author is with the Worcester Polytechnic Institute, Robotics Engineering, Worcester, MA 01609, USA. email: {gli7}@wpi.edu.

and specifically addresses the limitations posed by existing approaches that simplify system geometry. Methods that employ Euclidean Signed Distance Fields (ESDFs) result in discontinuous optimization constraints [13] while cylindrical obstacle representations limit the complexity of environments that can be modeled. We tackle these issues by formulating obstacle avoidance explicitly through polytopic models and represent each robot component and every obstacle as distinct polytopes. As we show in this work, this representation allows us to both incorporate smooth differentiable constraints into our global planner, and generate aggressive trajectories in tightly constrained environments.

To summarize, we present the following contributions:

- A novel non-conservative representation for aerial transportation that models the quadrotor, cable, and payload as separate polytopes. To enhance physical accuracy, we incorporate the attitude of both the robot and the obstacles into the environment representation, constructing orientation-aware polytopes that more accurately capture the system’s spatial footprint.
- An optimal global planning method for a robot composed of independent polytopes that produces collision-free trajectories in maze-like environments by leveraging duality theory to formulate non-linear polytopic collision constraints as smooth differentiable constraints.
- Experimental validation on hardware by performing real-world experiments using a quadrotor carrying a slung payload. We illustrate the advantages of our representation and planning method by tracking trajectories in tightly constrained environments. We also demonstrate that our approach generates faster trajectories than the existing state-of-the-art method in all eight test environments.

We plan to release our implementation as an open-source standalone package with minimal dependencies. Unlike other available frameworks that are integrated into extensive simulation environments, our package facilitates straightforward benchmarking and comparison, lowering the barrier to entry and accelerating innovation in planning and control for aerial transportation.

II. RELATED WORKS

In this section, we survey the main design choices in (i) how the environment and robots are spatially represented and (ii) how the states and inputs are mathematically modeled. We emphasize advancements that leverage polytopic geometry and highlight the benefits of PolyFly over prior works.

Environment Representations. Obstacle-aware planners typically encode the workspace either implicitly, through Exponential Signed Distance Fields (ESDFs), or explicitly, by representing obstacles with geometric shapes. Recent aerial transportation planners [6], [9], voxelize the environment and store an ESDF, turning collision checks into fast table look-ups. Although highly expressive, ESDFs can introduce non-smooth, discontinuous gradients, especially near object boundaries, affecting convergence in non-linear programs. As discussed in Section V-Q1, we believe this is one of the

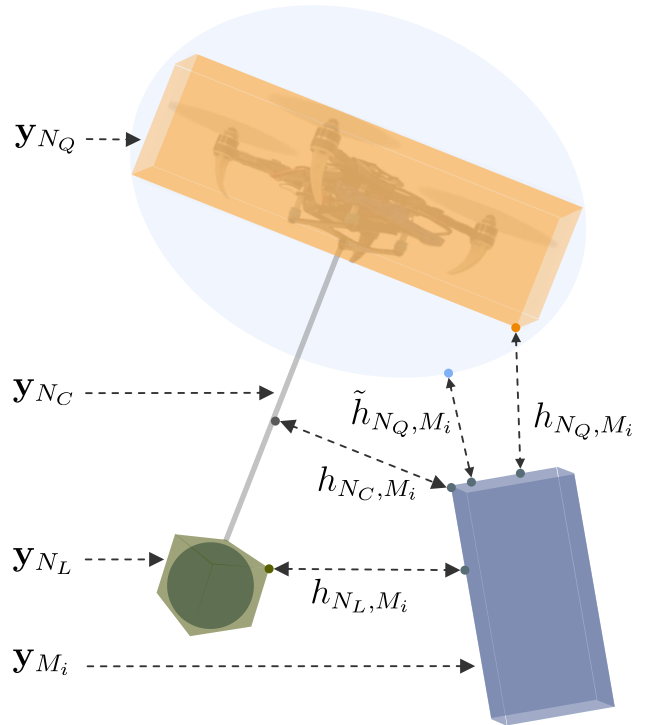


Fig. 2: System diagram showing the four different polytopes used in PolyFly: **Quadrotor** N_Q , **Payload** N_L , **Cable** N_C , and **Obstacles** M_i . The quadrotor polytope enables accurate distance computations h_{N_Q, M_i} , whereas most methods use an ellipse around the quadrotor resulting in conservative and inaccurate distance computations \tilde{h}_{N_Q, M_i} .

reasons such methods fail to converge and are outperformed by PolyFly.

Other works express the environment via geometric objects. [10]–[12] employ cylindrical and spherical objects, while [7], [8], [14] rely on polytopes. While ellipses and cylinders limit the range of scenes that can be modeled, polytopes significantly increase the complexity of environments that can be captured. In fact, works that use ESDFs also primarily consider environments composed of multiple cuboids [9]. Furthermore, in the context of trajectory planning, adopting polytopes to represent the environment yields distance constraints with good optimization properties. Duality theory can be used to convert non-linear polytope-to-polytope distance inequalities into smooth, differentiable constraints. [15], [16] used polytopic collision constraints for short-horizon reactive MPC frameworks but are unable to optimize over global paths due the short MPC horizon. [7] used this approach for global planning but did not consider complex environments and cannot navigate environments through narrow gaps, eg. Fig. 1, due to their conservative representation that models the robot as a single cuboid.

Spatial Robot Representation. There are two primary design decisions with respect to modeling the robot. First, how should the physical geometry of the robot be modeled? Existing methods typically use multiple spheres or ellipses

to represent the quadrotor and its payload [6], [9]–[12] or a single prism or polytope [7], [8]. These representations over-approximate at least one component (quadrotor, payload or cable), therefore limiting their applicability in highly constrained or cluttered environments. In contrast, our method addresses these limitations by leveraging orientation-aware polytopes for each robot component - quadrotor, cable, and payload. Combined with polytopic representation of the environments, we enable non-conservative distance evaluation, as shown in Fig. 2, facilitating aerial transportation in maze-like environments and narrow passages that are slightly larger than the width of the cable (see Fig. 5).

State and Input Modeling. The second design decision is how states and inputs are mathematically represented. A popular strategy is to express the states and inputs as polynomials to facilitate trajectory optimization [6], [9]. This is often paired with MINCO [17] to reformulate the problem into an unconstrained optimization to boost computational efficiency. While this approach can be used to achieve real-time capabilities, our experiments in Section V-Q1 indicate that it may compromise both solution quality and convergence. In contrast, similar to [7], [10]–[12], PolyFly operates directly in the native state space. Unlike polynomial parameterizations, the native state space approach places no restrictions on the shape of the state or control trajectories, making them inherently more expressive. Our experiments confirm that this added flexibility enables PolyFly to produce faster trajectories and tackle more complex environments than the state-of-the-art polynomial-based planner.

The methods presented in [6], [9], which serve as our baseline, employ an ESDF to represent the environment, approximate the quadrotor and payload with spheres, and parameterize the states and inputs via polynomials. [9] reports an ablation study comparing the computational times and success rates of their method with IPOPT-MP, a state-based global planning approach. However, they omit the comparison of the optimized trajectory times of their method with IPOPT-MP, and do not address navigation close to obstacles in maze-like environments. We demonstrate that by using the native state-based modeling and a non-conservative spatial workspace representation via polytopes, PolyFly outperforms the baseline in all test environments.

III. SYSTEM DYNAMICS

In this section, we summarize the non-linear dynamics of a quadrotor carrying a suspended payload. We follow the derivation presented in [3] and assume that the cable remains taut. Applying the Lagrange-d'Alembert principle, we obtain

$$\frac{d\mathbf{x}_L}{dt} = \dot{\mathbf{x}}_L, \quad \frac{d\mathbf{x}_Q}{dt} = \dot{\mathbf{x}}_Q, \quad \dot{\mathbf{q}} = \frac{1}{2}\hat{\boldsymbol{\Omega}}\mathbf{q}, \quad (1)$$

$$(m + m_L)(\ddot{\mathbf{x}}_L + \mathbf{g}) = (\boldsymbol{\xi} \cdot f\mathbf{R}_Q \mathbf{e}_3 - ml(\dot{\boldsymbol{\xi}} \cdot \dot{\boldsymbol{\xi}}))\boldsymbol{\xi}, \quad (2)$$

$$ml(\ddot{\boldsymbol{\xi}} + (\dot{\boldsymbol{\xi}} \cdot \dot{\boldsymbol{\xi}})\boldsymbol{\xi}) = \boldsymbol{\xi} \times (\boldsymbol{\xi} \times f\mathbf{R}_Q \mathbf{e}_3), \quad (3)$$

$$\mathbf{M} = \mathbf{J}\dot{\boldsymbol{\Omega}} + \boldsymbol{\Omega} \times \mathbf{J}\boldsymbol{\Omega}, \quad (4)$$

TABLE I: Notation table

\mathcal{I}, \mathcal{B}	inertial, and robot frame
m_L, m_Q	mass of payload and robot
$\mathbf{x}_L, \mathbf{x}_Q$	position of payload and robot in \mathcal{I}
$\dot{\mathbf{x}}_L, \ddot{\mathbf{x}}_L$	linear velocity, acceleration of payload in \mathcal{I}
$\ddot{\mathbf{x}}_L$	jerk of payload in \mathcal{I}
$\dot{\mathbf{x}}_Q, \ddot{\mathbf{x}}_Q$	linear velocity, acceleration of robot in \mathcal{I}
$\mathbf{R}_Q \in SO(3)$	robot orientation with respect to \mathcal{I}
$\boldsymbol{\Omega} \in \mathbb{R}^3$	angular velocity of robot in \mathcal{B}
$f \in \mathbb{R}, \mathbf{M} \in \mathbb{R}^3$	collective thrust and moment on robot in \mathcal{B}
$f_i \in \mathbb{R}$	i^{th} motor thrust
$J \in \mathbb{R}^{3 \times 3}$	moment of inertia of robot
$\boldsymbol{\xi} \in S^2$	unit vector from robot to payload in \mathcal{I}
$l, g \in \mathbb{R}$	cable length, gravity constant
\mathbf{q}	quaternion representation of \mathbf{R}_Q

$$\begin{bmatrix} f \\ \mathbf{M} \end{bmatrix} = \mathbf{D} \begin{bmatrix} f_1 \\ f_2 \\ f_3 \\ f_4 \end{bmatrix} \quad (5)$$

where $\mathbf{g} = g\mathbf{e}_3$, $g = 9.81 \text{ m/s}^2$, $\mathbf{e}_3 = [0 \ 0 \ 1]^\top$, and $\hat{\boldsymbol{\Omega}}$ is the skew-symmetric matrix of the quadrotor angular velocity $\boldsymbol{\Omega}$. Table I defines the remaining variables. The matrix \mathbf{D} provides a linear mapping between collective thrust-moments and individual motor thrusts. It is defined in terms of the robot's physical properties and propeller's aerodynamics characteristics. Readers can refer to [18] for additional information.

By leveraging the differential flatness property of the system [3], we can model the state dynamics described in eqs. (1)–(5) in terms of the flat outputs $\{\mathbf{x}_L, \psi\}$, where ψ is the quadrotor's yaw angle. In our method, we make the non-restrictive assumption and set $\psi = 0$. We choose to express the resulting dynamics as

$$\mathbf{x} = [\mathbf{x}_L^\top, \dot{\mathbf{x}}_L^\top, \ddot{\mathbf{x}}_L^\top]^\top, \mathbf{u} = [\ddot{\mathbf{x}}_L^\top]^\top. \quad (6)$$

The induced system dynamics are therefore modeled as a third-order integrator. Given \mathbf{x} , \mathbf{u} and the robot's physical parameters, we can use the non-linear differential flatness mapping [3] to calculate the robot position \mathbf{x}_Q , robot velocity $\dot{\mathbf{x}}_Q$, robot acceleration $\ddot{\mathbf{x}}_Q$ and robot orientation \mathbf{R}_Q . This allows our trajectory generator to plan in payload space and add constraints to the quadrotor's states. Since our planner operates in a discrete space, we convert the continuous time representation above to its discrete form. We obtain the Runge-Kutta approximation

$$\mathbf{x}(k+1) = F(\mathbf{x}(k), \mathbf{u}(k), \Delta t_k), \quad (7)$$

where F represents the discretized dynamics function and Δt_k the time step duration at stage k .

IV. PLANNING

A. Preliminaries

We develop a global planner that computes a collision-free trajectory τ for a quadrotor with a suspended payload where

$$\begin{aligned} \tau &= [\tau_0, \tau_1, \dots, \tau_N], \\ \tau_k &= [\mathbf{x}_L(k), \dot{\mathbf{x}}_L(k), \ddot{\mathbf{x}}_L(k)]^\top, \quad k \in (0, N). \end{aligned} \quad (8)$$

The robot starts at state \mathbf{x}_o and must navigate to its goal state \mathbf{x}_N . The environment is described by the set \mathbf{E} , which contains N_O polytopic obstacles M_i for $i \in (0, N_O)$. The aerial transportation system is modeled using three separate polytopes, N_j for $j \in \{Q, C, L\}$ that represent the quadrotor, cable, and load polytopes respectively, as shown in Fig. 2. The rest of this section discusses our choice of distance metric between the robot and obstacles, and a detailed overview of our optimization approach.

B. Polytopic Approximation

Let us consider two polytopes M_i and N_j , where M_i and N_j represent the obstacle and robot polytopes respectively, as defined in Section IV-A. Let \mathbf{y}_{M_i} be any point within the polytope M_i and \mathbf{y}_{N_j} be any point within the polytope N_j . $A_{M_i}, B_{M_i}, A_{N_j}$ and B_{N_j} are constants that define their geometric shape. These polytopes can be represented by the standard inequalities

$$\mathbf{A}_{M_i} \mathbf{y}_{M_i} \leq \mathbf{B}_{M_i}, \quad \mathbf{A}_{N_j} \mathbf{y}_{N_j} \leq \mathbf{B}_{N_j}. \quad (9)$$

While not strictly necessary, we simplify computation by representing one polytope's points in the other polytope's frame. We represent the obstacle points \mathbf{y}_{M_i} using the relative position vector $\mathbf{y}_{M_i}^{N_j}$, which gives

$$\mathbf{y}_{M_i} = \mathbf{R}_{N_j} \mathbf{y}_{M_i}^{N_j} + \mathbf{O}_{N_j}, \quad (10)$$

where \mathbf{R}_{N_j} is N_j 's rotation matrix, and \mathbf{O}_{N_j} is its origin. Substituting this into the polytopic form expressed by eq. (9), we can represent polytope M_i as

$$(\mathbf{A}_{M_i} \mathbf{R}_{N_j}) \mathbf{y}_{M_i}^{N_j} \leq \mathbf{B}_{M_i} - \mathbf{A}_{M_i} \mathbf{O}_{N_j}. \quad (11)$$

Since \mathbf{R}_{N_j} and \mathbf{O}_{N_j} are functions of the chosen state vector \mathbf{x} , M_i is represented by

$$(\mathbf{A}_{M_i} \mathbf{R}_{N_j}(\mathbf{x})) \mathbf{y}_{M_i}^{N_j} \leq \mathbf{B}_{M_i} - \mathbf{A}_{M_i} \mathbf{O}_{N_j}(\mathbf{x}), \quad (12)$$

$$= \mathbf{A}_{M_i}^{N_j}(\mathbf{x}) \mathbf{y}_{M_i}^{N_j} \leq \mathbf{B}_{M_i}^{N_j}(\mathbf{x}), \quad (13)$$

where $\mathbf{A}_{M_i}^{N_j}(\mathbf{x}) = \mathbf{A}_{M_i} \mathbf{R}_{N_j}(\mathbf{x})$ and $\mathbf{B}_{M_i}^{N_j}(\mathbf{x}) = \mathbf{B}_{M_i} - \mathbf{A}_{M_i} \mathbf{O}_{N_j}(\mathbf{x})$.

C. Distance Metric Between Polytopes

Our optimization problem seeks to lower bound h_{M_i, N_j} , the minimum signed distance between polytopes M_i and N_j , with a positive margin β . Specifically,

$$h_{M_i, N_j}(\mathbf{x}) \geq \beta, \quad h_{M_i, N_j}(\mathbf{x}) := sd(M_i, N_j), \quad (14)$$

where sd is the signed distance function described in [19], which is positive when sets M_i and N_j do not intersect, and negative when they do. The constraint defined by eq. (14) is non-differentiable and difficult to integrate into optimization problems when the obstacles and robots are represented as convex polytopes [19]. To handle this complexity, we follow the approach in [19] and reformulate eq. (14) using

duality theory into the following set of smooth non-linear differentiable constraints. The equivalent dual problem is

$$\begin{aligned} g_{M_i, N_j}(\mathbf{x}) &= \max_{\lambda_{N_j}, \lambda_{M_i}} -\lambda_{N_j}^\top \mathbf{B}_{N_j} - \lambda_{M_i}^\top \mathbf{B}_{M_i}^{N_j}(\mathbf{x}) \\ \text{s.t. } &\lambda_{N_j}^\top \mathbf{A}_{N_j} + \lambda_{M_i}^\top \mathbf{A}_{M_i}^{N_j}(\mathbf{x}) = 0 \\ &\lambda_{M_i} \geq 0, \quad \lambda_{N_j} \geq 0, \quad \|\lambda_{M_i} * \mathbf{A}_{M_i}\|_2 \leq 1 \end{aligned} \quad (15)$$

Results in [19], [20] show that Strong Duality holds for the dual problem defined in eq. (15), which gives us the lower bound of the primal cost function $h_{M_i, N_j}(\mathbf{x})$

$$\bar{g}_{M, N}(\mathbf{x}, \lambda_{M_i}, \lambda_{N_j}) := -\lambda_{N_j}^\top \mathbf{B}_{N_j} - \lambda_{M_i}^\top \mathbf{B}_{M_i}^{N_j}(\mathbf{x}) \leq h_{M_i, N_j}(\mathbf{x}). \quad (16)$$

Therefore, to enforce the minimum signed distance of β between M_i and N_j , we constrain the lower bound $\bar{g}_{M, N} \geq \beta$, which gives us smooth non-conservative reformulation of eq. (14) as

$$\begin{aligned} &-\lambda_{N_j}^\top \mathbf{B}_{N_j} - \lambda_{M_i}^\top \mathbf{B}_{M_i}^{N_j}(\mathbf{x}) \geq \beta, \\ &\lambda_{N_j}^\top \mathbf{A}_{N_j} + \lambda_{M_i}^\top \mathbf{A}_{M_i}^{N_j}(\mathbf{x}) = 0, \\ &\lambda_{M_i} \geq 0, \quad \lambda_{N_j} \geq 0, \quad \|\lambda_{M_i} * \mathbf{A}_{M_i}\|_2 \leq 1. \end{aligned} \quad (17)$$

We add the set of constraints defined in eq. (17) for collisions between each (M_i, N_j) pair, where $i \in (0, N_O)$.

D. Optimization Problem Formulation

Our planner solves the following optimization problem

$$\begin{aligned} \min_{\mathbf{x}(k), \mathbf{u}(k), \Delta t(k)} &\sum_{k=0}^{N-1} L(\mathbf{x}(k), \mathbf{u}(k), \Delta t(k)) \\ \text{subject to } &\mathbf{x}(k+1) = F(\mathbf{x}(k), \mathbf{u}(k), \Delta t(k)), \\ &\mathbf{x}(0) = \mathbf{x}_0, \quad \mathbf{x}(N) = \mathbf{x}_N, \\ &H_l(\mathbf{x}(k), \mathbf{u}(k)) \leq 0, \quad \forall l \in (0, N_h), \end{aligned} \quad (18)$$

where N is the horizon length, k is the stage index, $\Delta t(k)$ is the time duration for stage k , and x_0 and x_N are the initial and terminal states respectively. H_l comprises the N_h inequality constraints from the collision-avoidance formulation in eq. (17) together with the state and input bounds specified in Section IV-D.7. $L = L_t + L_u + L_g + L_{td}$ is the loss function defined later in this subsection. The optimization constraints, costs and initialization are discussed below.

1) *Time Minimization*: We incentivize the planner to minimize the total trajectory time by adding a large cost to each time step duration. Specifically,

$$L_t = \frac{\alpha_{to}}{N} \sum_{k=0}^{N-1} \Delta t_k, \quad (19)$$

$$\Delta t_{min} \leq \Delta t_k \leq \Delta t_{max},$$

where $\Delta t_{min}, \Delta t_{max}, \alpha_{to} > 0$.

2) *Input Smoothness Regularization*: We add a small cost that penalizes large changes between consecutive inputs, thereby regularizing their rate of change and improving the smoothness of the resulting robot states.

$$L_u = \frac{\alpha_u}{N} \sum_{k=1}^N \|\mathbf{u}_i - \mathbf{u}_{i-1}\|^2, \quad \alpha_u > 0. \quad (20)$$

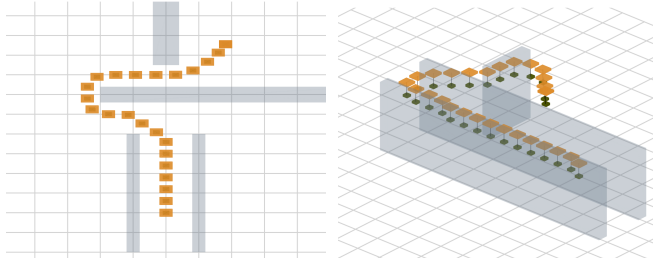


Fig. 3: A* initialization of trajectories for Env. 6 (left) and Env. 8 (right)

3) *Regularizing Proximity to the Initial Guess*: Even though we use a simple A* initialization, we expect the optimal trajectory's positions to lie in the vicinity of the initialized positions. We achieve this by adding a small penalty to deviations of the optimized positions from the initial guess. The study supporting the benefits of this term is discussed in Section V-Q4.

$$L_g = \frac{\alpha_g}{N-1} \sum_{k=1}^{N-1} \|\mathbf{x}(k) - \mathbf{x}_g(k)\|^2, \quad (21)$$

where $\mathbf{x}_g(k)$ is the initial guess at stage index k and $\alpha_g > 0$.

4) *Regularizing Subsequent Time Step Durations*: We add a small cost to the difference between subsequent time step durations to help our solver converge. Specifically, we add the following cost term

$$L_{td} = \frac{\alpha_{td}}{N} \sum_{k=0}^{N-1} \|\Delta t_{k+1} - \Delta t_k\|^2, \quad \alpha_{td} > 0. \quad (22)$$

5) *Solver Initialization*: Since the optimization problem combines non-linear dynamics with non-convex collision constraints, the resulting solution is sensitive to its initial guess. Whereas many prior planners [6], [9] adopt a kinodynamic initialization strategy, our approach begins from a simple A* path that ignores the non-linear dynamics and assumes the cable is always aligned with the global z -axis, i.e., $\ddot{\mathbf{x}}_L = 0$. Fig. 3 visualizes this initialization for two representative environments. We then use a lightweight initialization method for the load velocities using the equation

$$\dot{\mathbf{x}}_{L,k} = \frac{\mathbf{x}_{L,k+1} - \mathbf{x}_{L,k}}{\Delta t_{max} - \Delta t_{min}}. \quad (23)$$

Even with this relatively simple initialization method, our planner produces high quality trajectories that are consistently better than the baseline.

6) *Collision Constraints*: We account for the collision between the quadrotor, cable, and payload polytopes against each obstacle. For each time stage k and each polytope pair, we add the constraints derived in Section IV-C. As an example, to handle collisions between the payload polytope N_L and an obstacles M_i , we add the following constraints

for all stages k and obstacles i

$$\begin{aligned} \forall k, \forall i \quad & -\lambda_{N_L,k}^\top \mathbf{B}_{N_L} - \lambda_{M_i,k}^\top \mathbf{B}_{M_i}^{N_L}(\mathbf{x}_k) \geq \beta, \\ & \lambda_{N_L,k}^\top \mathbf{A}_{N_L} + \lambda_{M_i,k}^\top \mathbf{A}_{M_i}^{N_L}(\mathbf{x}_k) = 0, \\ & \lambda_{M_i,k} \geq 0, \quad \lambda_{N_L,k} \geq 0, \quad \|\lambda_{M_i,k} * \mathbf{A}_{M_i}\|_2 \leq 1. \end{aligned} \quad (24)$$

7) *State and Input Constraints*: The initial and final positions are of the quadrotor and payload are specified based on the environment and are enforced via equality constraints

$$\mathbf{x}(0) = \mathbf{x}_0, \quad \mathbf{x}(N) = \mathbf{x}_N. \quad (25)$$

We constrain the start and end velocities, accelerations and jerks to zero to account for hardware limitations as

$$\dot{\mathbf{x}}_L(0) = \dot{\mathbf{x}}_L(N) = 0, \quad \ddot{\mathbf{x}}_L(0) = \ddot{\mathbf{x}}_L(N) = 0, \quad (26)$$

$$\dot{\mathbf{x}}_Q(0) = \dot{\mathbf{x}}_Q(N) = 0, \quad \ddot{\mathbf{x}}_Q(0) = \ddot{\mathbf{x}}_Q(N) = 0, \quad (27)$$

$$\mathbf{u}(0) = \mathbf{u}(N) = 0. \quad (28)$$

Finally, we bound the state and inputs based on the robot's limitations and the environment dimensions.

$$\mathbf{x}_l \leq \mathbf{x} \leq \mathbf{x}_h, \quad \mathbf{u}_l \leq \mathbf{u} \leq \mathbf{u}_h. \quad (29)$$

8) *Incorporating the Quadrotor's Rotation into the Polytopic Constraints*: To improve the accuracy of the polytopic representation, we rotate the quadrotor polytope by the quadrotor's rotation. Due to the system's differential flatness property, given \mathbf{x} and \mathbf{u} , we can derive the robot's rotation \mathbf{R}_Q and use it to compute the $\mathbf{A}_{M_i}^{N_Q}$ matrix in eq. (13)

V. EXPERIMENTAL RESULTS

We conduct various experiments to evaluate the capabilities of this method. We seek to answer the following questions:

- Q1** Can this planning method produce trajectories that navigate tightly around corners of polytopic obstacles in cluttered maze environments?
- Q2** What are the benefits of modeling each component of the robot separately?
- Q3** What are the benefits of adding the quadrotor's orientation into the polytopic representation?
- Q4** Is adding a cost that regularizes the proximity to the initial guess important?
- Q5** Does our velocity initialization method help the solver converge?
- Q6** Can we run these aggressive trajectories on a real quadrotor with a suspended payload?

Q1 Navigating Cluttered Environments

We create 8 maze environments to evaluate the performance of our planning method. The optimization problem is constructed in CasADi [21] and solved it with IPOPT [22]. We compare our method against the MINCO approach [17] adopted in [6], [9] by utilizing their open-source code. To ensure a fair comparison, we adjust the baseline's safety margins, ESDF map resolution, kinodynamic search resolution, and quadrotor parameters to be consistent with our environment setup. Furthermore, for each environment,

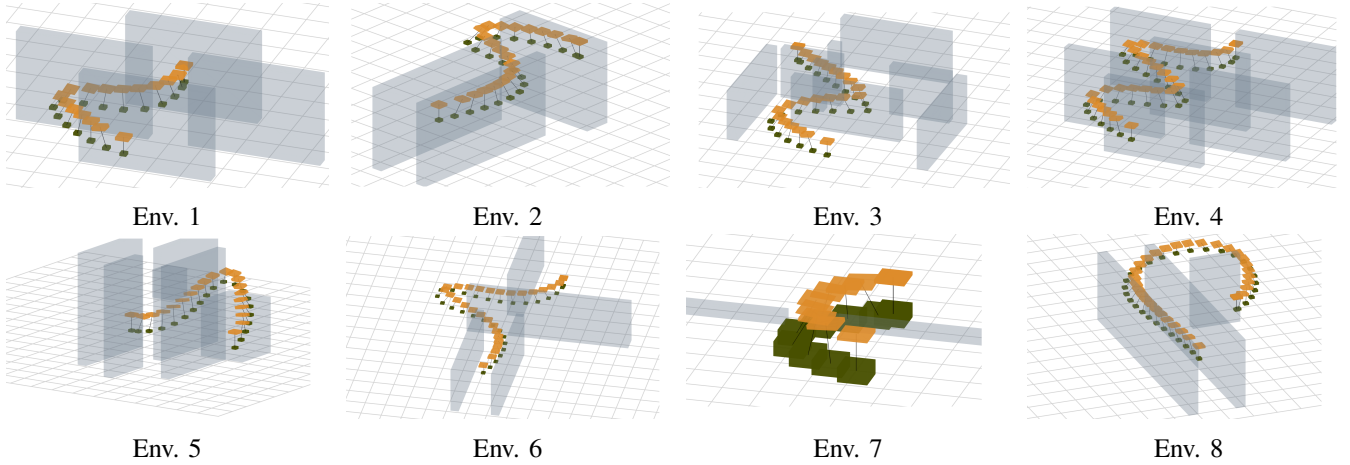


Fig. 4: Visualization of optimized trajectories using PolyFly in 8 tightly cluttered environments. The **quadrotor** is in yellow, **payload** in green, **cable** in gray and **obstacles** in light blue

we tune the baseline’s and PolyFly’s time minimization weights and report the best results in Table II. The optimized trajectories for our method in each environment are shown in Fig. 4.

The baseline method fails to produce a collision-free trajectory for 3/8 environments, as indicated by the \times symbol. We also observed that in some environments, the baseline generated shorter paths in terms of distance, yet required more time to traverse them. This indicates that our method is able to better optimize for total flight time, even if that entails following a slightly longer path at higher speeds. Across all test environments, PolyFly successfully generates paths where the robot tightly navigates around obstacles and aggressively cuts corners to maximize global performance. This boost in performance compared to the baseline partly stems from the geometric modeling of the workspace and the use of the dual formulation, which produces smooth, non-conservative collision constraints [19]. These properties enable the solver to plan paths that safely steer around obstacles while maintaining speed.

TABLE II: PolyFly vs. Baseline [6]. Time is total trajectory time and Path is the total path length. \times marks a failure.

Env.	PolyFly		Baseline [6]		% Faster
	Time (s)	Path (m)	Time (s)	Path (m)	
1	3.92	4.46	4.10	4.45	4.1
2	5.02	7.17	\times	\times	∞
3	4.95	6.65	5.68	6.47	12.3
4	7.17	8.81	7.47	8.74	4.3
5	4.20	5.74	4.30	4.92	6.3
6	5.45	8.08	6.43	8.02	15.7
7	3.16	3.05	\times	\times	∞
8	4.93	9.42	\times	\times	∞

Q2 Independent Polytopic Models for Robot Components

Modeling each robot component as a separate polytope allows the trajectory generator to accurately represent the system’s geometry. This fidelity is important when producing

agile trajectories in tightly constrained environments, where the robot must cut corners aggressively while still avoiding obstacles. Moreover, the dual formulation of polytopic avoidance yields smooth, non-conservative constraints [19], in contrast to the baseline ESDF approaches, whose gradients can be non-smooth and discontinuous.

The advantage is evident in Env. 7, where the robot must pass through a narrow opening wider than the cable but thinner than the payload and quadrotor. Our method successfully produces a trajectory that threads the cable through the gap, allowing the robot to safely navigate the environment. The real world experiment snapshots are shown in Fig. 1. The baseline fails to produce a feasible trajectory, likely due the geometric over-approximation and non-smooth gradients induced by the ESDF.

Q3 Incorporating the Quadrotor’s Rotation Into Polytopic Representation

Accurately capturing the quadrotor’s rotation further increases the fidelity of the polytopic model and therefore navigation reliability. This detail becomes critical when the vehicle flies close to a ceiling, particularly for a platform with long rotor arms that forms a thin yet wide rectangular footprint. Since high-acceleration maneuvers induce large attitude changes, aggressive trajectories close to overhead surfaces can cause rotor collisions with the environment. As shown in Fig. 2, most planners approximate the vehicle as an ellipse, which is an over-approximation of the robot body, especially for large frames. By employing a tight polytope that explicitly accounts for the robot’s rotation, we eliminate this conservatism and ensure collision free navigation in near-ceiling flight.

We demonstrate these benefits in a scenario where the quadrotor must fly just below a ceiling. Fig. 6 illustrates how incorporating the orientation into the planner prevents collisions. In Fig. 6 (A), the quadrotor strikes the ceiling during a high-acceleration maneuver because the planner ignores the attitude change that accompanies acceleration. In

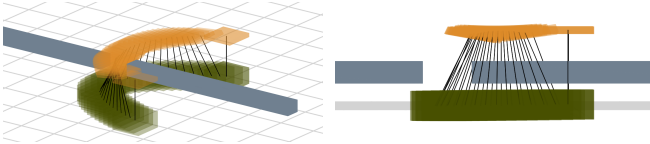


Fig. 5: Close up visualizations of the optimized trajectories through a narrow gap in Env. 7.

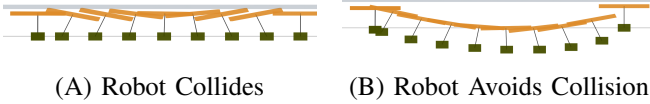


Fig. 6: Impact of incorporating quadrotor rotation in the polytopic model. Left: A rotation-agnostic planner produces a trajectory that collides with the ceiling. Right: By accounting for the robot’s attitude, the optimized path descends to prevent collisions while accelerating.

contrast, Fig. 6 (B) shows how the orientation-aware planner descends during the acceleration phase to avoid a collision.

Q4 Regularizing Proximity to Initial Guess

We perform an ablation study to determine if regularizing the proximity to the initial guess is important. For each environment, we run the optimizer with 3 different α_g values. The results are shown in Table III.

TABLE III: Trajectory time [s] for different values of α_g . A \times indicates a failure to generate a collision-free trajectory.

Env.	$\alpha_g = 0$	$\alpha_g = 1$	$\alpha_g = 5$
1	\times	3.92	3.92
2	\times	5.01	5.02
3	\times	3.94	4.95
4	\times	\times	7.17
5	4.07	4.67	4.20
6	\times	5.42	5.45
7	3.16	3.16	3.16
8	\times	5.01	4.93

PolyFly fails in 6/8 environments if $\alpha_g = 0$ and in 1/8 environments when $\alpha_g = 1$. For $\alpha_g = 5$, the optimizer succeeds in all environments. This highlights the value of this regularization term. We believe this aids convergence by incentivizing the optimizer to remain in the vicinity of the initial guess, preventing it from entering regions of local minima that are difficult to escape from.

Q5 Payload Velocity Initialization

To evaluate the effectiveness of our solver initialization strategy, we conduct an ablation study that compares the payload-velocity initialization of eq. (23) against a variant where velocities are initialized to zero. Table IV summarizes the results.

The solver fails in 3/8 environments without the velocity initialization strategy. For all other scenarios, our strategy on average significantly reduces the number of required solver iterations by roughly 45%.

TABLE IV: Performance with and without velocity initialization across environments. A \times indicates optimization failure.

Env.	With Velocity Initialization		W/o Velocity Initialization	
	Traj Time (s)	Iterations	Traj Time (s)	Iterations
1	3.92	226 \downarrow	3.93	418
2	5.02	411 \downarrow	4.63	494
3	4.95	117 \downarrow	\times	\times
4	7.17	169 \downarrow	7.14	756
5	4.20	402 \downarrow	4.20	698
6	5.45	307 \downarrow	\times	\times
7	3.16	104 \downarrow	3.18	126
8	4.93	192 \downarrow	4.94	597

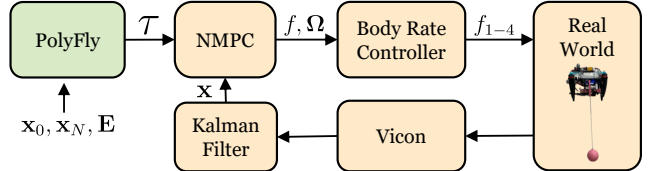


Fig. 7: System architecture for real-world deployment.

Q6 Real World Experiments

We run several real world experiments with environments 1, 3 and 7 to validate that our method produces trajectories that can be deployed on real robots. An overview of our system architecture is shown in Fig. 7. The desired \mathbf{x}_L , $\dot{\mathbf{x}}_L$, \mathbf{x}_Q and $\dot{\mathbf{x}}_Q$ are sent to a Non-Linear Model Predictive Controller (NMPC) that runs onboard the robot at 200 Hz. The NMPC uses the dynamics model presented in eqs. (1)–(5) with inputs f_{1-4} . We extract the NMPC’s expected thrust and bodyrates and send them to a low-level PX4 controller. The robot’s states are measured using an external motion capture system and are upsampled using onboard Kalman Filters.

Snapshots of our experiments are shown in Fig. 1. The position tracking errors for the quadrotor and payload are shown in Fig. 8 and Table V. Our results indicate that PolyFly produces dynamically feasible trajectories that can be tracked by an onboard controller with low errors. The supplementary video contains additional real-world footage that highlights the agile trajectories generated by our method.

TABLE V: Tracking error statistics

Axis	Error (m)	Env. 1	Env. 3	Env. 7
x	Mean	0.027	0.029	0.021
	Std	0.017	0.016	0.094
y	Mean	0.058	0.059	0.052
	Std	0.047	0.048	0.036
z	Mean	0.024	0.039	0.029
	Std	0.012	0.029	0.087

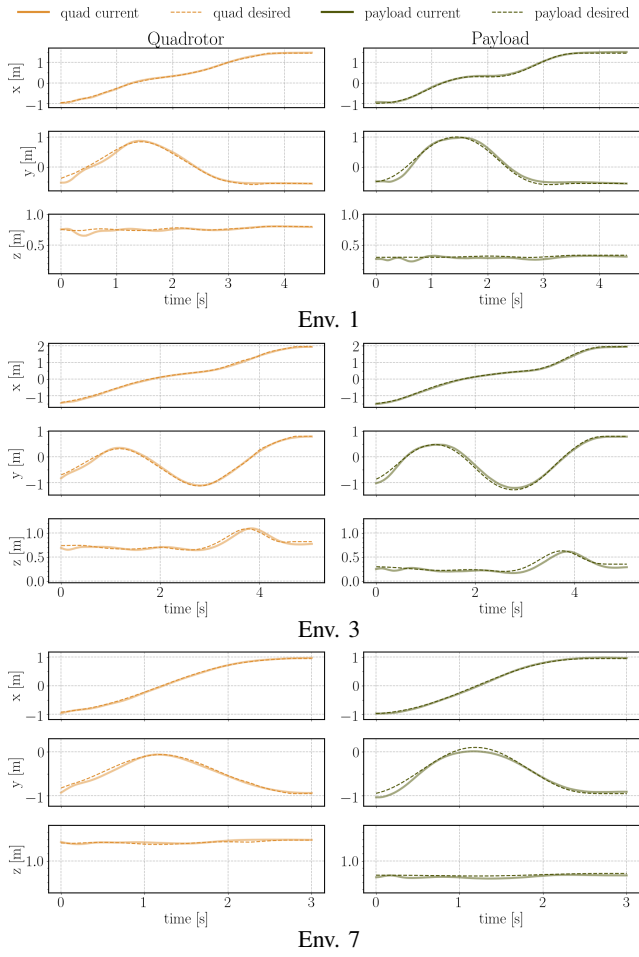


Fig. 8: Desired vs. Measured positions of the quadrotor and payload during real-world experiments for Env. 1, 3 and 7.

VI. CONCLUSION

This paper presented PolyFly, a global planner for a single robot aerial transportation system that models the robot and environment using a set of polytopes and enables the generation of collision-free trajectories in cluttered scenarios. Our proposed method yielded consistently faster trajectories than a popular state-of-the-art baseline in eight different maze-like environments. Experimental results also confirm the trajectories' dynamic feasibility and applicability of the proposed solution in real-world settings. Future works will explore how the global trajectories can be efficiently updated upon receiving local obstacle information through onboard sensors. We would also like to leverage the latest advances in accelerating polytopic collision avoidance checks [23] to reduce computation.

REFERENCES

- [1] M. A. Trujillo, J. R. Martinez-de Dios, C. Martin, A. Viguria, and A. Ollero, “Novel aerial manipulator for accurate and robust industrial ndt contact inspection: A new tool for the oil and gas inspection industry,” *Sensors*, vol. 19, no. 6, 2019.
- [2] G. Loianno and V. Kumar, “Cooperative transportation using small quadrotors using monocular vision and inertial sensing,” *IEEE Robotics and Automation Letters*, vol. 3, no. 2, pp. 680–687, April 2018.
- [3] K. Sreenath, T. Lee, and V. Kumar, “Geometric control and differential flatness of a quadrotor uav with a cable-suspended load,” in *52nd IEEE Conference on Decision and Control (CDC)*, 2013, pp. 2269–2274.
- [4] E. N. Barmpounakis, E. I. Vlahogianni, and J. C. Gofias, “Unmanned aerial aircraft systems for transportation engineering: Current practice and future challenges,” *International Journal of Transportation Science and Technology*, vol. 5, no. 3, pp. 111–122, 2016.
- [5] T. A. Rodrigues, N. L. O. Jay Patrikar, H. S. Matthews, S. Scherer, and C. Samaras, “Drone flight data reveal energy and greenhouse gas emissions savings for very small package delivery,” *Patterns*, 2022.
- [6] H. Li, H. Wang, C. Feng, F. Gao, B. Zhou, and S. Shen, “Autotrans: A complete planning and control framework for autonomous uav payload transportation,” *IEEE Robotics and Automation Letters*, vol. 8, no. 10, pp. 6859–6866, 2023.
- [7] J. Zeng, P. Kotaru, M. W. Mueller, and K. Sreenath, “Differential flatness based path planning with direct collocation on hybrid modes for a quadrotor with a cable-suspended payload,” *IEEE Robotics and Automation Letters*, vol. 5, no. 2, pp. 3074–3081, 2020.
- [8] S. Tang and V. Kumar, “Mixed integer quadratic program trajectory generation for a quadrotor with a cable-suspended payload,” in *2015 IEEE International Conference on Robotics and Automation (ICRA)*, 2015, pp. 2216–2222.
- [9] H. Wang, H. Li, B. Zhou, F. Gao, and S. Shen, “Impact-aware planning and control for aerial robots with suspended payloads,” *IEEE Transactions on Robotics*, vol. 40, pp. 2478–2497, 2024.
- [10] C. Y. Son, H. Seo, D. Jang, and H. J. Kim, “Real-time optimal trajectory generation and control of a multi-rotor with a suspended load for obstacle avoidance,” *IEEE Robotics and Automation Letters*, vol. 5, no. 2, pp. 1915–1922, 2020.
- [11] P. Foehn, D. Falanga, C. Luethi, M. Achtelik, R. Siegwart, and D. Scaramuzza, “Fast trajectory optimization for agile quadrotor maneuvers with a cable-suspended payload,” in *Robotics: Science and Systems XIII*, N. Amato, S. Srinivasa, N. Ayanian, and S. Kuindersma, Eds. Cambridge, Massachusetts, USA: RSS Foundation, July 2017.
- [12] C. Y. Son, D. Jang, H. Seo, T. Kim, H. Lee, and H. J. Kim, “Real-time optimal planning and model predictive control of a multi-rotor with a suspended load,” in *International Conference on Robotics and Automation (ICRA)*, 2019, pp. 5665–5671.
- [13] J. Schulman, Y. Duan, J. Ho, A. Lee, I. Awwal, H. Bradlow, J. Pan, S. Patil, K. Goldberg, and P. Abbeel, “Motion planning with sequential convex optimization and convex collision checking,” *The International Journal of Robotics Research*, vol. 33, no. 9, pp. 1251–1270, 2014.
- [14] G. Yu, D. Cabecinhas, R. Cunha, and C. Silvestre, “Aggressive maneuvers for a quadrotor-slung-load system through fast trajectory generation and tracking,” *Autonomous Robots*, vol. 46, no. 4, pp. 499–513, Apr. 2022.
- [15] A. Pallar, G. Li, M. Sarvaiya, and G. Loianno, “Optimal trajectory planning for cooperative manipulation with multiple quadrotors using control barrier functions,” *arXiv preprint arXiv:2503.01096*, 2025.
- [16] A. Thirugnanam, J. Zeng, and K. Sreenath, “Safety-critical control and planning for obstacle avoidance between polytopes with control barrier functions,” in *International Conference on Robotics and Automation (ICRA)*, 2022, pp. 286–292.
- [17] Z. Wang, X. Zhou, C. Xu, and F. Gao, “Geometrically constrained trajectory optimization for multicopters,” *IEEE Transactions on Robotics*, vol. 38, no. 5, pp. 3259–3278, 2022.
- [18] T. Lee, M. Leok, and N. H. McClamroch, “Geometric tracking control of a quadrotor uav on $se(3)$,” in *49th IEEE Conference on Decision and Control (CDC)*, 2010, pp. 5420–5425.
- [19] X. Zhang, A. Liniger, and F. Borrelli, “Optimization-based collision avoidance,” *IEEE Transactions on Control Systems Technology*, vol. 29, no. 3, pp. 972–983, 2020.
- [20] S. Boyd and L. Vandenberghe, *Convex Optimization*. Cambridge, UK: Cambridge University Press, 2004.
- [21] J. A. E. Andersson, J. Gillis, G. Horn, J. B. Rawlings, and M. Diehl, “CasADi – A software framework for nonlinear optimization and optimal control,” *Mathematical Programming Computation*, vol. 11, no. 1, pp. 1–36, 2019.
- [22] A. Wachter and L. T. Biegler, “On the implementation of an interior-point filter line-search algorithm for large-scale nonlinear

programming,” *Mathematical Programming*, vol. 106, no. 1, pp. 25–57, Mar. 2006.

[23] Z. Wu, Z. Wang, and H. Zhang, “Gpu-accelerated optimization-based collision avoidance,” in *IEEE International Conference on Robotics and Automation (ICRA)*, 2024, pp. 7561–7567.